CHALMERS
UNIVERSITY OF TECHNOLOGY

The numerical simulation of standard concrete tests and steel reinforcement using force flux peridynamics

Received: 16 February 2022 | Revised: 4 April 2022 | Accepted: 6 May 2022

DOI: 10.1002/suco.202200153

ARTICLE

fib CEB-FIP WILEY

The numerical simulation of standard concrete tests and steel reinforcement using force flux peridynamics

Jens Olsson[1] | **Mats Ander**[2] | **Chris J. K. Williams**[1]

[1]Department of Architecture and Civil Engineering, Architectural Theory and Methods, Chalmers University of Technology, Göteborg, Sweden

[2]Division of Material and Computational Mechanics, Department of Industrial and Materials Science, Chalmers University of Technology, Göteborg, Sweden

Correspondence
Jens Olsson, Department of Architecture and Civil Engineering, Architectural Theory and Methods, Chalmers University of Technology.
Email: jens.olsson@chalmers.se

Funding information
Svenska Forskningsrådet Formas; VINNOVA

Abstract

Peridynamics is a numerical particle-based solid mechanics method that enables the simulation of brittle and quasi-brittle materials, as well as ductile materials. It allows cracking to appear spontaneously in the arms joining the particles and can therefore be used to simulate progressive fracture. In this article, we apply our version of peridynamics, which we call force flux peridynamics, to the simulation of concrete where the appearance of cracks plays an important role in the global mechanical properties. It is not difficult to modify the material parameters in peridynamics to achieve a given tensile strength or a given compressive strength. However, it is much more difficult to choose parameters which will model all the strength parameters of a material within the same model. When concrete fails in compression it may split or spall showing a complex relationship between compressive and tensile failure. We therefore set ourselves the simple task of producing a single peridynamics model which can predict the stiffness and strength behavior of concrete in standard compression and tension tests for which we chose the American Society for Testing and Materials standards for the cylinder compression test, the split cylinder test, and the modulus of rupture test. A parameter sensitivity study was performed based on the cylinder compression test to tune the key peridynamics parameters that determine the global material behavior. The compressive and tensile strengths were then determined from the combined simulation data. While the fracture modes, crack branching pattern and also the stress–strain curve show promising results, the maximum tensile strength was found to be significantly larger than physical experiments suggest. This is probably due to imperfections within real concrete at the interface between aggregate particles and cement paste and it shows that the detailed numerical modeling of the failure of concrete is highly complex with a large number of unknown material parameters.

Discussion on this paper must be submitted within two months of the print publication. The discussion will then be published in print, along with the authors' closure, if any, approximately nine months after the print publication.

KEYWORDS
concrete fracture, concrete simulation, concrete strength, force flux peridynamics, material testing, SPH

1 | INTRODUCTION

In simple terms, we design concrete structures so that the concrete works in compression and tensile stresses are resisted by reinforcement, which is usually steel, and may or may not be prestressed. However, it is not as simple as that because in order to transfer forces from the concrete to the reinforcement we rely on bond stresses, producing shear and tension in the concrete. Thus, the tensile strength of concrete is at least as important as its compressive strength, but because concrete is a brittle or quasi-brittle material its tensile strength is less than its compressive strength and is very much influenced by stress concentrations, including preexisting shrinkage cracks and the interface between aggregate particles and the cement paste. Thus, there is a need for theoretical and numerical models to use the results from simple standard material tests to predict how concrete will behave in these situations where tensile strength is important and where the geometry and stress state are complex.

The concrete also functions to protect the steel from moisture which can find its way to the steel reinforcement through small cracks in the covering concrete layer, hence the prediction of fracture in concrete becomes highly important topic for structural safety, both in terms of sudden failure and long term durability. Recent development in machine learning suggest new approaches to detect appearance of cracks with image processing.[1] The understanding of how fracture develops in concrete structures is mostly derived from physical experiments. But such experiments are time consuming, expensive and typically carried out on simple objects like beams and columns, making the knowledge difficult to generalize to a more arbitrary design case.

Concrete simulation techniques are typically classified based on scale in groups of microscopic, mesoscopic, and macroscopic techniques. Macroscopic techniques typically smear the properties of sand, aggregate, and cement paste into a homogeneous material either based on a discrete approach such as the random particle model[2] or based on a continuous approach where the fracture process is approximated as a dissipation at the material level, where the cracks are diffused as micro-cracks. The random particle method would appear to be very similar to peridynamics, and predates it, but peridynamics is the more commonly used term today. At the Mesoscale, concrete is typically modeled as a three-component mix, large aggregates, cement paste and the bonding interface between the two. Mesoscale models are widely used in the modeling of concrete fracture because it enables the study of effects where the proportions of the three-component mixes are varied just like in the real material. They also enable the study of effects from initiated micro cracks and the coalesces of the micro-cracks to form major defects in the material which may contribute to the failure, see.[3] The family of microscopic techniques further extend the level of detail in the modeling of concrete to capture all the constituents of the mix. The models can be created through a type of random distribution aided with computational techniques such as Voronoi diagrams or from real concrete samples through x-ray Computed Tomography images.[4]

Recent development of computer-based simulation techniques such as peridynamics and smooth particle hydrodynamics has shown the ability to predict progressive fracture in a variety of brittle materials,[5] including concrete.[6] Following the introduction of peridynamics by Stewart Silling in 2000[7] Gerstle et al.[8,9] introduced micropolar peridynamics by adding a pairwise moment to the bond based formulation to tackle poission's ratio limitations and apply it for modeling of concrete. The same approach is later used by Yaghoobi and Chorzepa for the analysis of fiber reinforced concrete.[10] Huang, Sheng et al.[11–13] work along the same trajectory and simulate crack propagation and failure modes for concrete with bond based peridynamics. An extensive review of peridynamics for modeling brittle materials written by Javili can be found in[5] and for the application to concrete, the most recent work is summarized in a review article by Hattori et al.[14]

Simulation of concrete using Smooth Particle Hydrodynamics (SPH) is typically more focused on impact problems, such as bullet-slab penetration in Reference 15 and missile impact in Reference 16 and concrete fragmentation in Reference 17. Other implementations include modeling of fiber reinforced concrete Reference 18 and flow simulation of self-compacting concrete in Reference 19.

In the study presented here, a numerical meshless method called Force Flux Peridynamics (FFPD) derived in Reference 20 based on SPH and Peridynamics, is extended to 3D simulations and applied to concrete fracture modeling for the first time. The varying particle sizes capabilities with FFPD makes it an attractive choice in the real design scenario, where different parts of a model can be

represented with suitable accuracy. Although FFPD could be used for modeling at different scales it is applied here as a macroscopic technique. The purpose of working with a macroscopic technique is to provide a method that can be used in a realistic design situation. Although the meso and micro scales techniques may represent simulations of fracture more accurately, they are inherently difficult to apply in a design situation, due to the complexity of the setup resulting from the requirement in precision for the representation of the concrete material in its various constituent parts. Macro models, on the other hand, do not attempt to model the individual constituents but just capture the global behavior which becomes more suitable for a design case. Therefore, this study aims to the explore fracture prediction enabled with FFPD in a macro setup of concrete modeling for structural design. But before the model can be applied in a design scenario the material parameters for concrete need to be tuned which is the main focus of this study.

The tuning of the numerical concrete model is approached through a parameter sensitivity study based on the cylinder compression test which can be seen in Figure 1. The parameters that control the brittleness of concrete are chosen to recreate a high strength concrete with a compressive strength of approximately 60 MPa. The same numerical model is then used for the split cylinder test to estimate the tension strength. Initial puzzling results lead to the additional modeling of the modulus of rupture and direct tension test, inspired by Raphael's study[21] of concrete tension strength where the same set of tests were used.

The results from the parameter sensitivity study of the compression test show great capabilities of modeling different characteristic stress strain curves, which could represent different concrete mixes. The results from the tension tests, on the other hand, indicate a material model which is significantly stronger than expected. That could be explained through the lack of imperfections in the material, calling for further investigation.

It should be noted that in peridynamics the continuum properties of a material arise out of thousands of interactions between individual particles. The average properties, such as density or Young's modulus, are quite easy to model, but fracture involves the progressive failure of the material, when it is much more difficult to relate the bulk properties[22] to the interaction between particles. For this reason yield in steel is much easier to model than fracture of concrete and Figures 26 and 27 show results from such an analysis using FFPD. Of course the modeling of the transfer of force between concrete and steel is yet more challenging.

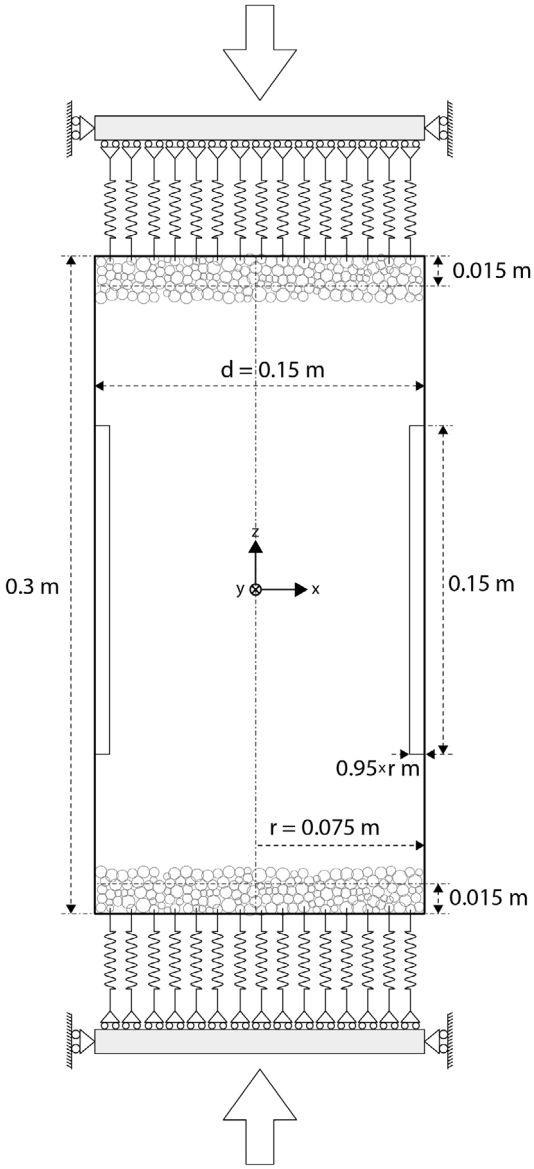

FIGURE 1 Setup for the compression concrete cylinder test. The neoprene caps used in the physical test to distribute the load evenly are modeled here using a spring bed on each side of the cylinder.

2 | TESTING CONCRETE

The first standards for testing concrete strength was developed in 1917 by the American Society for Testing and Materials (ASTM). Since then two main standards have developed, the cylinder test and the cube test. The cylinder test has been used for this study because the same shape of sample can be used for both compression and tension tests.

The difficulty in evaluating the tensile strength of concrete has been highlighted by Hannant in 1973 in a study of aggregate size effects on the split cylinder test.[23] Jerome Raphael further developed Hannant's findings with a comprehensive study of data from 12,000 concrete

tension tests. The purpose was to develop explanations for the variation in the tensile strength that was recorded from the split cylinder, the modulus of rupture and the direct tension test.[21] Raphael concluded that the splitting strength was about 10% of the compressive strength.

2.1 | Cylinder test

The specimen in a concrete cylinder test has a diameter of 150 mm and a height of 300 mm based on the ASTM standards as described.[24] A vertically oriented cylinder is used for the evaluation of compressive strength. The cylinder is placed at the center of a hydraulic press which applies a load to produce a rate of stress 0.15–0.35 MPa/s. To provide a uniform load distribution, neoprene caps can be used in between the hydraulic press disc and the two ends of the concrete cylinder. The numerical setup of this test is illustrated in Figure 1.

2.2 | Split cylinder (Brazilian) test

The difficulty of applying pure tension to concrete has led to the popularization of a tension strength testing technique called the split cylinder test,[25] which also goes under the name the Brazilian test with reference to Carneiro.[26] The cylindrical specimen has the same dimensions as in the compression test and a detailed setup can be found.[27] The tension stress is introduced to the specimen via a diametrically applied compressive force as shown in Figure 2. The simplicity of the split cylinder test and the fact that testing equipment from the compression test can be used has made it a widely used for concrete strength testing.

If concrete is assumed to be a linear elastic material, and that the conditions of plane stress apply, then the theory of elasticity[28] predicts a uniform tensile stress acting horizontally on the vertical plane between the lines along which the load is applied. The cylinder therefore splits in two halves when the load is increased. The numerical setup for the simulation of the cylinder test is shown in Figure 2.

2.3 | Modulus of rupture

The modulus of rupture test estimates the tensile strength from a transverse bending test, in which a simply supported beam-like specimen with rectangular cross-section is loaded by one or two point loads, to give a 3 or 4 point test. As with the split cylinder test, the tensile stress is calculated from the load using a theory from applied mechanics, in this case the Euler-Bernoulli theory of

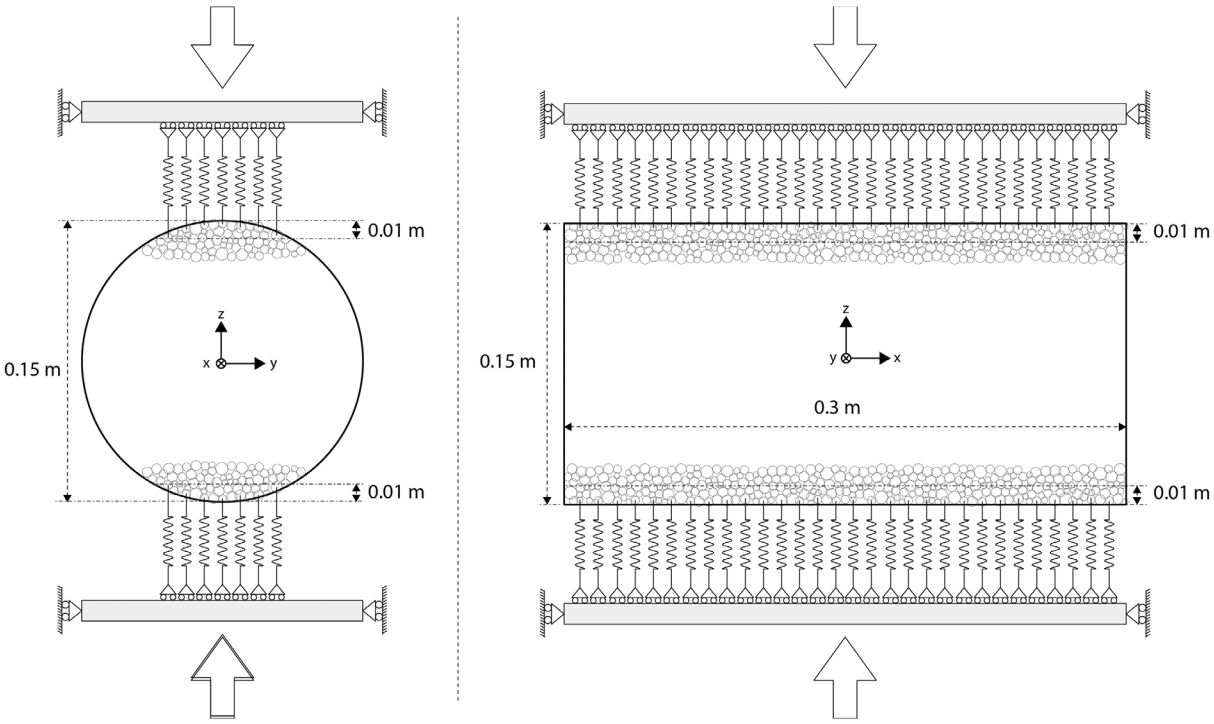

FIGURE 2 Setup for the split cylinder test. The gradually thickened boundary zone that is achieved with each horizontal slice of the cylindrical object results in a gradually increasing load intensity towards the center of the specimen.

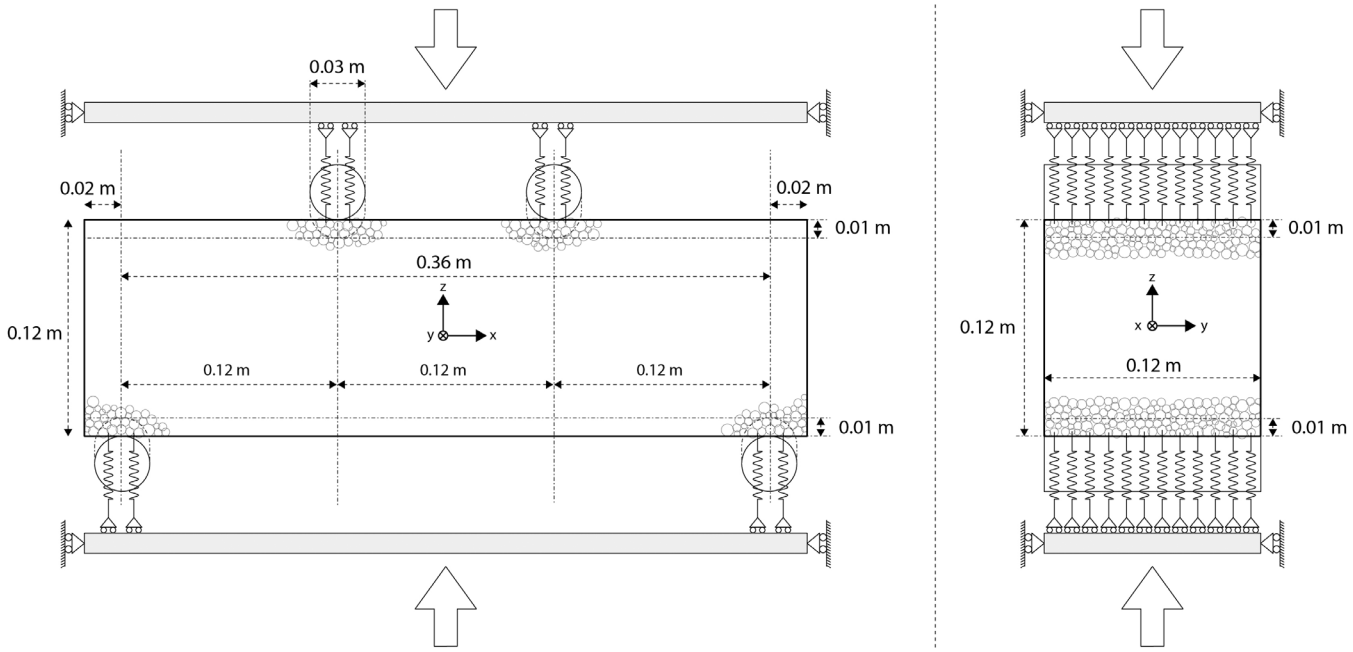

FIGURE 3 Setup for the modulus of rupture test. The cylinders that are used to load the specimen in the physical test are used to select the particles for the application of boundary conditions.

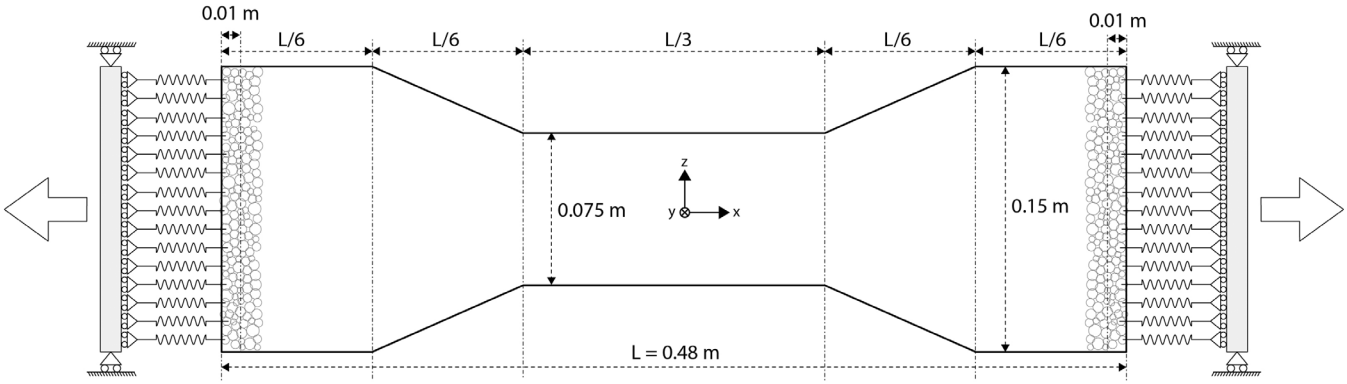

FIGURE 4 Setup for the direct tension test. The dimensions are chosen so that the volume is similar to the other tests.

bending of beams. The maximum tensile stress occurs at the bottom of the beam where the bending moment is maximum. Thus, the maximum tensile stress is more localized than it is in the split cylinder test. The numerical setup for the simulation of the modulus of rupture test is illustrated in Figure 3.

2.4 | Direct tension for concrete and steel

A direct tension test is simple in theory but more complicated in practice. A cylindrical or rectangular specimen is clamped at each of its two ends, which are slowly pulled apart to induce tension stress in the object. It is challenging to ensure that the stress is applied in a uni-axial fashion and it is therefore not a commonly used test for concrete, and ASTM does not provide a recommended standard.[29] However, the challenging boundary conditions are largely overcome in a numerical setup and a homemade version of the direct tension test is include as a third means of testing tensile strength, see Figure 4. Another direct tesion test is used for the simulation of steel reinforcement, see Figure 5.

3 | FORCE FLUX PERIDYNAMICS

This section will present the most important features of the Force Flux Peridynamcis (FFPD) theory that is used for the simulations presented in section 2 and 4. For the

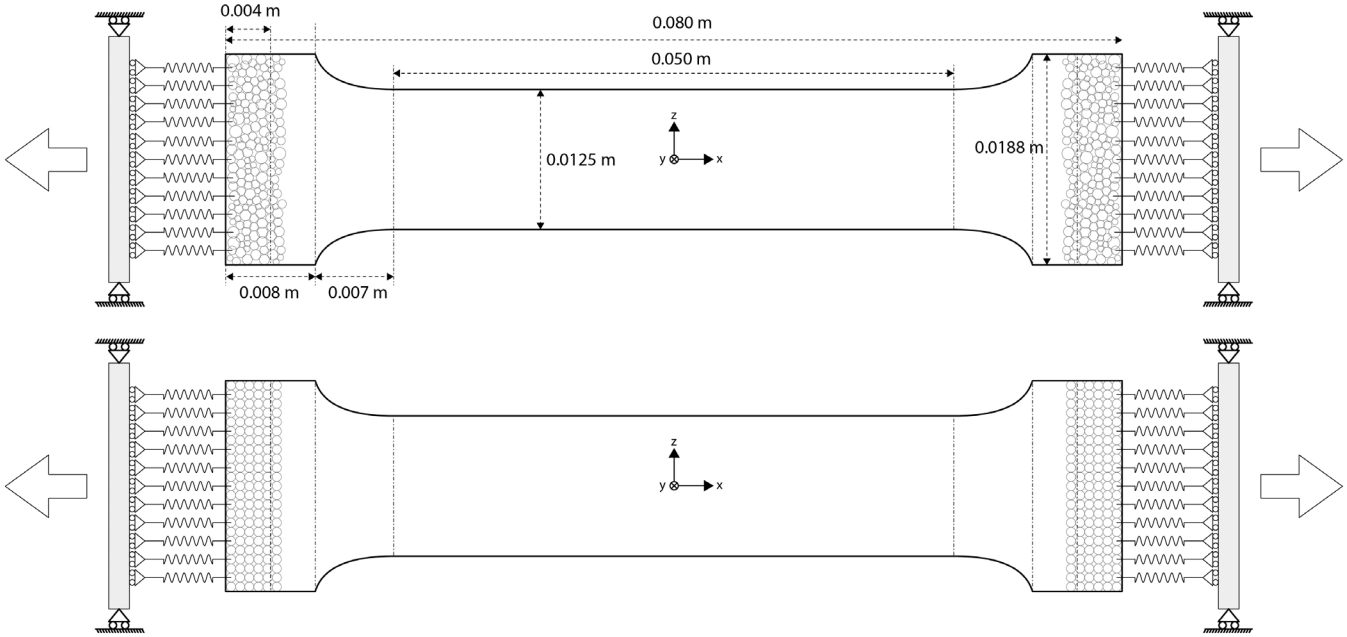

FIGURE 5 Setup for the ASTM 370 test for steel reinforcement where the irregular particle distribution is illustrated above the regular particle distribution.

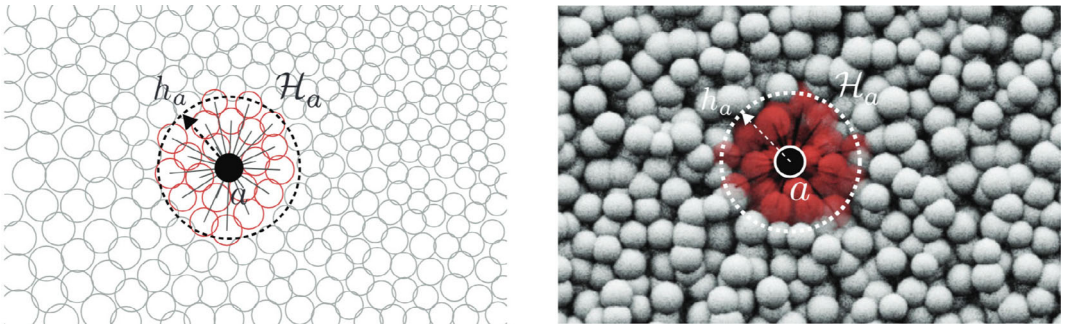

FIGURE 6 A rectangular sub region of a FFPD continuum in 2D and 3D with varying sized particles. The arms are drawn for a particle a within the horizon domain H_a which is defined by the radius h_a.

full derivation of the theory, the reader is referred to Reference 20.

Peridynamics is a non-local continuum theory that was developed for the simulation of fracture phenomenon for brittle materials and was introduced by Silling in 2000.[7] Unlike classical continuum mechanics, peridynamics does not require cracks to be predefined but allows cracking to appear spontaneously from an initial intact domain. Again unlike classical continuum mechanics which relies on the evaluation of partial derivatives, peridynamics works by replacing the differentiation with integration which remains valid also in the presence of discontinuities. FFPD presents an alternative formulation of the original Peridynamics theory and simplifies the use of variable particle sizes and irregular particle distribution. This is achieved by merging concepts from Smooth Particle Hydrodynamics (SPH)[30] with the Peridynamics theory[7,31] as shown in Reference 20. The bond force in FFPD is reformulated to allow for different size particles while enabling an arbitrary Poisson's ratio and modeling of ideal plastic deformation. The FFPD continuum is approximated with a finite set of particles with intermediate arms. Each particle P_a is connected by arms to the neighboring particles within a distance h_a which defines a horizon $\mathcal{H}$ which is circular in 2D and spherical in 3D, as illustrated in Figure 6.

3.1 | Force flux density

The most central concept in FFPD is the force flux density, S, which is defined as a function of the state of stress

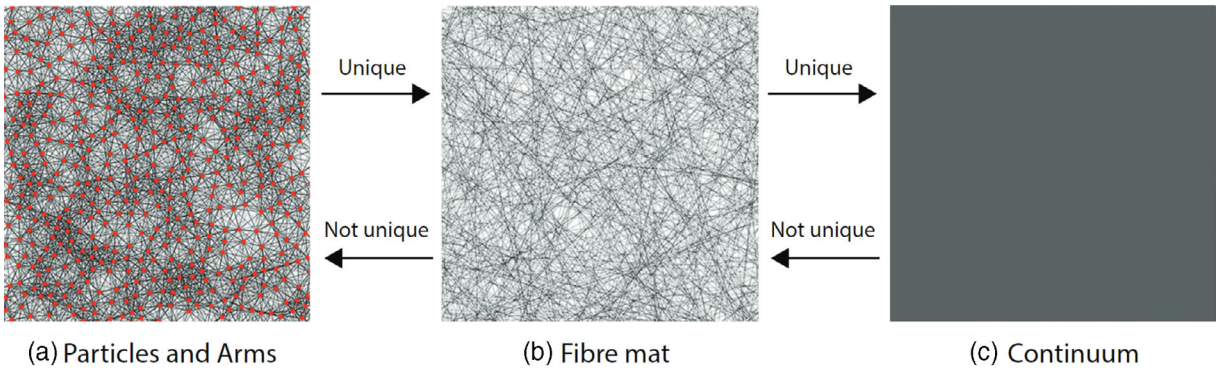

FIGURE 7 Discrete particles and arms on the left, fiber mat in the center and continuum to the right. Knowledge of the arm forces implies a unique set of fiber tension and compression which implies a unique stress in the continuum. But the reverse does not apply.

and the fiber orientation relative to that state of stress. In 3D it is given by:

$$S = \frac{2\pi}{3} TL, \tag{1}$$

where T is the tension [N] in each fiber in a particular direction and L is the total length of the fibers per unit volume. L has units length per unit volume, or one over length squared $\left[\frac{1}{m^2}\right]$. Therefore, S has the dimensions of stress [Pa]. The tension T in a single fiber as shown in Figure 7b, is then calculated as:

$$T = \frac{3S}{2\pi L}, \tag{2}$$

according to equation (14) in Reference 20 for the 3D case. To prepare for the discrete setup illustrated in Figure 2a, the state of stress needs to be formulated based on a direction vector $\boldsymbol{q}$. We also want to separate the deviatoric and volumetric parts of the stress, $\boldsymbol{\tau}$ and $\overline{\sigma}$, respectively. Following the derivation in Reference 20 (section 3), Equation (2) takes the form:

$$T = \frac{3}{2\pi L}\left(\frac{5}{2}\mathbf{q}\cdot\boldsymbol{\tau}\cdot\mathbf{q} + \overline{\sigma}\right). \tag{3}$$

To finally introduce the discrete particles and arms into this fibremat-model we introduce the SPH kernel function W and the weighting of particle size in terms of mass m and density ρ. The formula for the tension in a discrete arm between particles a and b is then given by:

$$T_{ab} = -\frac{m_a m_b}{\rho^2}\left(\frac{\partial W_{ab}}{\partial r_{ab}} + \frac{\partial W_{ba}}{\partial r_{ab}}\right)\left(\frac{5}{2}\mathbf{q}_{ab}\cdot\boldsymbol{\tau}\cdot\mathbf{q}_{ab} + \overline{\sigma}\right), \tag{4}$$

where $\frac{\partial W_{ab}}{\partial r_{ab}}$ is the derivative of the kernel function with respect the unit vector, r_{ab}, along the arm. The particle masses and kernel functions in Equation (4) are now defined separately for particles a and b, enabling variable parameters and thus variable particle distribution in the domain approximation. The kernel that is defined in section 10.1 in Reference 20 is used also for this implementation, with $k = 2$ and $\alpha = 4.5$.

The constitutive relation based on shear modulus G and bulk modulus K is introduced in the force flux expression in equation (110) in Reference 20. For the 3D case when $N = 3$ the expression for S at particle a can be written as:

$$S_a(\mathbf{q}_{ab}) = 5G\left(\epsilon_{ab} - \epsilon_{ab}^{\text{plastic}}\right) + (3K - 5G)\overline{\epsilon}_a, \tag{5}$$

where ϵ_{ab} is the total engineering strain calculated using Pythagoras' theorem, $\epsilon_{ab}^{\text{plastic}}$ is the plastic strain and $\overline{\epsilon}_a$ is the mean strain. By inserting Equation (5) in Equation (3) the final expression for the arm force is given as:

$$T_{ab} = -\frac{m_a m_b}{\rho^2}\left(\frac{\partial W_{ab}}{\partial r_{ab}} + \frac{\partial W_{ba}}{\partial r_{ab}}\right)\left(5G\left(\epsilon_{ab} - \epsilon_{ab}^{\text{plastic}}\right) + (3K - 5G)\overline{\epsilon}_a\right). \tag{6}$$

The last thing that needs to be added to complete this ideal plastic fracture model is a failure condition. Arm failure in the original peridynamics formulation is defined based on a strain limit which does not work in FFPD since variable arm lengths are introduced. Griffith's theory of fracture postulates that the failure stress σ_{failure} is related to the crack width c, the Young's modulus E and the surface energy γ according to:

$$\sigma_{\text{failure}} \approx \sqrt{\frac{2E\gamma}{c\pi}}. \tag{7}$$

We then write the surface energy as $\gamma = \delta\sigma_{\text{yield tension}}$, where δ is a constant length which is related to the

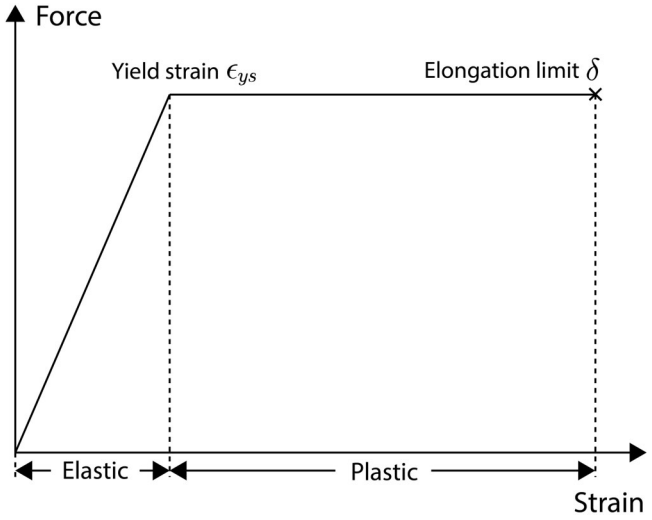

FIGURE 8 Ideal plastic model for the individual arms. The yield strain is measured as a percentage of the arm length whereas the plastic elongation limit is a constant length parameter independent of arm length.

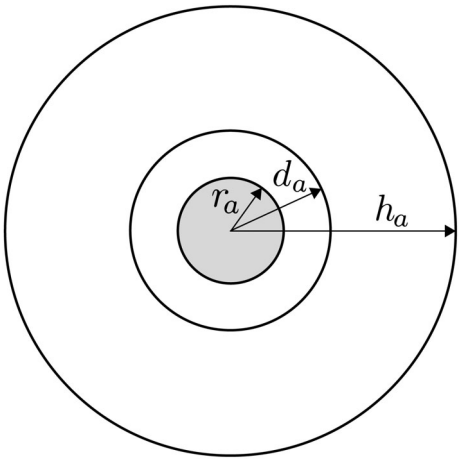

FIGURE 9 Three definitions for the size of a particle a, where r_a represents the size base on mass, volume and density for the material, d_a is a size used to define the number of close proximity neighbors and h_a represent the radius of the horizon of connectivity as shown in Figure 6.

amount of deformation associated with the surface energy. This length scale is independent of the initial length of the arms. That means short arms will require a greater strain to reach fracture than long arms. The complete derivation of the theory can be found in Reference 20.

4 | NUMERICAL SETUP OF THE PHYSICAL TESTS

Figures 1–4 illustrate the numerical setup for the simulation of the compression cylinder, the split cylinder, the modulus of rupture and the direct tension test. Each figure contains the relevant dimensions needed to reproduce the numerical experiment. The dimension are chosen to first and foremost follow the ASTM standard for the compression cylinder and split cylinder test according to References 24 and 27. The specimen proportions of the modulus of rupture test are also base on the ASTM standards according to Reference 32 but the size is tuned so that it has the same volume as the cylinder specimens. Since there is no ASTM standard for the direct tension test a cylinder with a waist was used and configured to have the same volume as the other test cases. Because of the way the particles are distributed, as explained in Section 4.1, the exact number of particles will vary slightly for each test case.

The selection of the boundary particles that are used to transfer load on to the test specimen varies a little depending on the test setup. For the cylinder compression and the direct tension test, the boundary particles are selected by introducing a limit in the z or x direction such that a slice of the specimen on each side becomes part of the boundary zone. Each particle in the boundary zone is then connected to a spring which is loaded by gradually displacing the plate on each side of the specimen in the direction of the large arrows, see Figures 1 and 4. For the split cylinder test a similar type of z limit is used to select all particles above and below a certain height. The varying thickness of the top and bottom slice in the boundary zone results in a gradually increasing load intensity as y in Figure 2 approaches 0. The boundary particles for the modulus of rupture test are furthermore selected by moving the four loading cylinders in the z-direction towards the center-line of the beam, see Figure 3, and each particle that falls inside a cylinder is assigned to be a boundary particle. The resulting boundary regions are thicker just below or above the center of each loading cylinder, similar to the case of the split cylinder, and thus the load is applied in a non-abrupt way.

For each of the four test cases the bounding box (cylinder, rectangular box etc.) is divided into a number of zones to improve computational process of setting up the topological connectivity, that is, which particle is connected to which neighboring particle. The long side of the cylinder is for example divided into 10 zones, and the two short sides in five zones each, giving a total of 250 zones. Further details on zoning, particle and arm count can be found in Table 2. But before the particle connectivity can be established the particle distribution and size calculations need to be done.

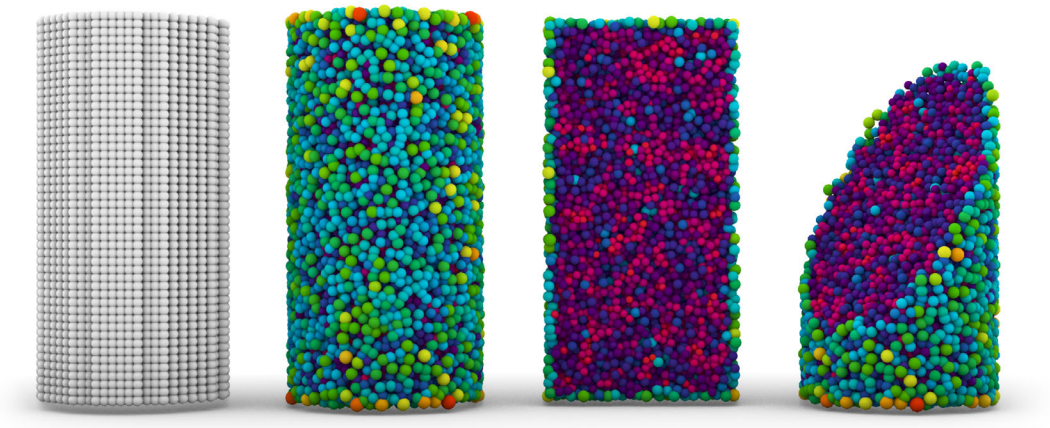

FIGURE 10 The particle distribution illustrated where the spheres represent the mass-size r for each particle in the cylinder, before and after the shaking and the size update. The regular starting grid is illustrated to the left and the irregular distribution to the right. The boundary effects that result from particle size calculation in algorithm 2 described in Figure 12 are clearly seen in the two rightmost images with larger particles on the surface of the cylinder and the largest particles at the surface edge.

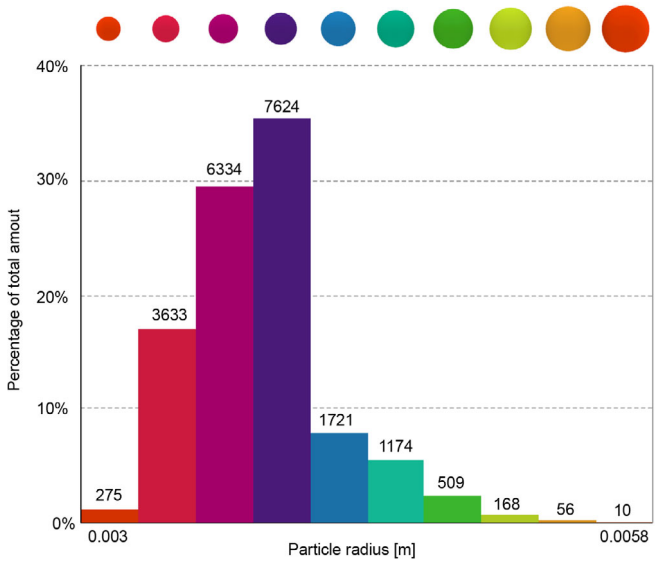

FIGURE 11 The particle mass-size distribution for the cylinder model where the particle radius r_a is divided in 10 different domains ranging from 0.003 to 0.0058 m in radius.

Algorithm 1 Shaking particles to introduce noise in the regular distribution

for $(k \in \{0, \ldots, 100\})$ **do**
  for $(i \in \{0, \ldots, \text{nParticles-1}\})$ **do**
    $\boldsymbol{p}_a \leftarrow particles[i]$
    $\boldsymbol{v}_{rnd} \leftarrow 0.2d_a|(x_{rnd}, y_{rnd}, z_{rnd})|$
    $\boldsymbol{p}_{a,new} \leftarrow \boldsymbol{p}_a + \boldsymbol{v}_{rnd}$
    nNeig $\leftarrow$ number of neighbouring particles closer then $h_a$form $\boldsymbol{p}_a$
    for $(j \in \{0, \ldots, \text{nNeig-1}\})$ **do**
      $\boldsymbol{p}_b \leftarrow particles[j]$
      overlap $\leftarrow (r_a - r_b) - |\boldsymbol{p}_{a,new} - \boldsymbol{p}_b|$
      if (overlap $< 0.75r_a$) **then**
        $\boldsymbol{p}_a = \boldsymbol{p}_{a,new}$
      end if
    end for
  end for
end for

Algorithm 2 Calculating the size of the particles for irregular distribution

$rNeig \leftarrow$ define required number of neighbours, we use 6.
for $(k \in \{0, \ldots, 20\})$ **do**
  for $(i \in \{0, \ldots, \text{nParticles-1}\})$ **do**
    $nNeig \leftarrow$ find the number of neighbours closer then d_a
    $diff \leftarrow (rNeig - nNeig)$
    $d_a \leftarrow d_a + 0.0001 diff$
    $r_a \leftarrow d_a/2$
    $h_a \leftarrow r_a\alpha$
  end for
end for

FIGURE 12 Algorithms 1 and 2 are described in procedural pseudo code.

4.1 | Random generation of the particle configuration

In order to describe the procedure for how to distribute the particles an approach needs to be establish for how to estimate the size of the particles. The first step is to generate a regular grid of particles, calculate the total volume V of the object (for example the cylinder), and divide that volume equally over all the particles. A particle radius r_a, also referred to as the mass-size, can then be obtained from the particle volume V_a using:

$$r_a = \sqrt[3]{\frac{3V_a}{4\pi}}, \tag{8}$$

assuming that the particle has a spherical shape. The mass-size is illustrated in 3D in Figure 10 and the mass size distribution is also shown as a bar graph in Figure 11. The initial regular arrangement of the particles is then distorted through a shaking procedure to introduce noise. The procedure is described in algorithm 1 in Figure 12 and is based on a Monte Carlo simulation.

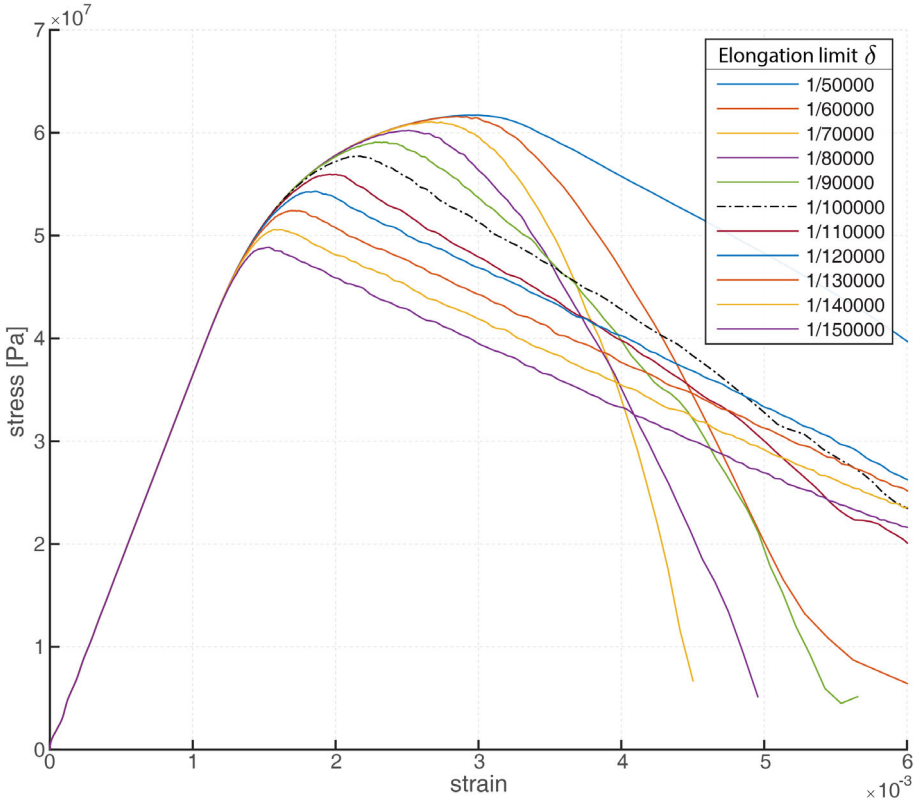

FIGURE 13 Stress-strain curves obtained from the concrete cylinder compression test with 10 different values for the plastic elongation limit δ.

Concrete		**Steel**	
$\nu = 0.2$	$E = 40$ GPa	$\nu = 0.28$	$E = 210$ GPa
$\rho = 2400$ kg/m^3	$\boldsymbol{\delta = 1e^{-5}\, m}$	$\rho = 7800$ kg/m^3	$\boldsymbol{\delta = \{1e^{-3}, ..., 1e^{-4}\}}$ **m**
$\boldsymbol{\alpha = 4.5}$	$\boldsymbol{\epsilon_{ys} = 1/800}$	$\alpha = 4.5$	$\boldsymbol{\epsilon_{ys} = \{1e^{-3}, ..., 5e^{-3}\}}$
$k = 2$	$G = 16.6$ GPa	$k = 2$	$G = 8.2$e10GPa
$L_{\text{spring}} = 0.01$ m	$K = 22.2$ GPa	$L_{\text{spring}} = 0.01$ m	$K = 1.6e11$ GPa
$k_{\text{spring}} = 3 \times 10^6$ N/m	$\Delta t = 2 \times 10^{-6}$ s	$k_{\text{spring}} = 3 \times 10^6$	$\Delta t = 8 \times 10^{-9}$ s

TABLE 1 Parameters used for setting up the material properties for the concrete and the steel

Note: Parameters in bold and varied in the parameter sensitivity study.

Each of the equally spaced particles are moved along a scaled random vector in an iterative fashion for 100 iterations. If the movement of a particle results in less than a 75% overlap with the closest neighboring particles and the particle is still inside the bounding box of the object (for example the cylinder), the movement is accepted. Otherwise the particle stays at the previously given position. Parameters (such as overlap allowance and movement magnitude) are tuned to reach a movement successes rate of approximately 20–30%. The procedure is describe in pseudo code in algorithm 1 explained in Figure 12 where $x_{rnd}, y_{rnd}, z_{rnd}$ refer to x, y, z values generated with a random function (in this case the *srand()* function from the C++ stdlib.h library). After the noise has been introduced to the regular particle arrangement the size of the particles need to be updated. This is a little more complicated with an irregular particle distribution. A base-size d is introduced and assigned to each particle as a doubling of the mass-size, such that $d_a = 2r_a$, see Figure 9. Since all particles had the same mass-size radius from the regular setup they will all have the same base-size too. In order to adjust the sizes, a target number of close proximity neighbors is defined to be 6, which is half of the number of neighbors in a close-packing of equal spheres where the neighbor count is 12. The size update algorithm is run for 20 iterations to reach a reasonable convergence and the procedure is described in algorithm 2 which is shown in Figure 12.

After the noise has been introduced and the particle sizes has been updated the arms need to be created. This

TABLE 2 Parameters used for setting up the geometry for the concrete and steel simulations

Compression cylinder	
Zone count = (8 4 4) = 128	Arms per particle ≈ 77
Arm count = 937697	Container volume ≈ 0.00530 m^3
Particle count = 21504	Used load steps = 1512
Split cylinder	
Zone count = (8 4 4) = 128	Arms per particle ≈ 77
Arm count = 1070642	Container volume ≈ 0.00530 m^3
Particle count = 24450	Used load steps = 1227
Modulus of rupture	
Zone count = (12 4 4) = 192	Arms per particle ≈ 70
Arm count = 1043847	Container volume ≈ 0.00535 m^3
Particle count = 26400	Used load steps = 1222
Direct tension	
Zone count = (12 4 4) = 192	Arms per particle ≈ 76
Arm count = 1043161	Container volume ≈ 0.00530 m^3
Particle count = 24128	Used load steps = 1302
Steel test (settings used for all 80 simulations)	
Zone count = 256	Arms per particle ≈ 76
Arm count = 433156	Used load steps ≈ 55000
Particle count = 11392	

is done by connecting each particle p_a with all the neighboring particles p_b within the distance of h_a which is the radius of the horizon.

The whole setup of the model is summarized following these six steps:

1. Particles are generated with equal spacing to create a regular grid.
2. Particles that do not lie inside the object container are removed.
3. Initial size estimate of r, d are calculated based on the container volume and a regular particle distribution.
4. Noise is introduced by shaking the particles for 100 iterations according to algorithm 1 described in Figure 12.
5. Particle sizes r, d and h are updated by running algorithm 2 which is described in Figure 12 for 20 iterations.
6. The arms are created by connecting each particle with all neighbors within a distance h.

5 | LIMITATIONS

There are several limitations to this study that are worth to be mentioned and motivated. Firstly the work presented here is limited to the numerical study of concrete and no physical testing is performed. In that way, we do not have a particular concrete mix to replicate but try to capture the phenomena of concrete failure on a more general level. However, some parameter need to be fixed to study the effects on varying the other parameters and the choices become a little arbitrary without having a real concrete to replicate.

The ambition behind the study is furthermore to create a simple rules in the small scale (particle and arm) to recreate a complex behavior in the large scale. Therefore, we have limited ourselves to an ideal plastic model of the arms without strain softening, which can be seen to still reproduce a softening behviour in the larger scale which can be seen in Figure 13. More elaborate model can be implemented with relative ease for further studies.

We have not dealt specifically with the reduced stiffness for the particles on the free surfaces which have fewer neighbors compared with an internal particle. The reasoning it again to keep the model as simple as possible. The influence of the weight for each specimen is further more neglected since it has little significance in relation to the external load.

6 | NUMERICAL EXPERIMENTS

The numerical experiments section contains six parts. The first part is a brief note on the numerical solver and the second part is an introduction to the parameters that are used in all the concrete simulations, also listed in Table 1. The third part includes a sensitivity study for the parameters that control the brittleness of the concrete. The compression cylinder as shown in Figure 1 is used for this purpose with the parameters from Tables 1 and 2. At the end of this section the selected choice of parameters are listed. Some additional results, which indicate how well the model can reproduce the Young's modulus and the Poisson's ratio, are also presented. The forth part includes the results from the simulations for the four different tests. These are then compiled together in the comparative summary which is the fifth and last part of this section that concerns concrete. The final part then contains a re-adaption of the concrete simulation to simulate steel reinforcement.

6.1 | Numerical solver

The numerical experiments are performed using simulation assuming quasi-static conditions with an explicit

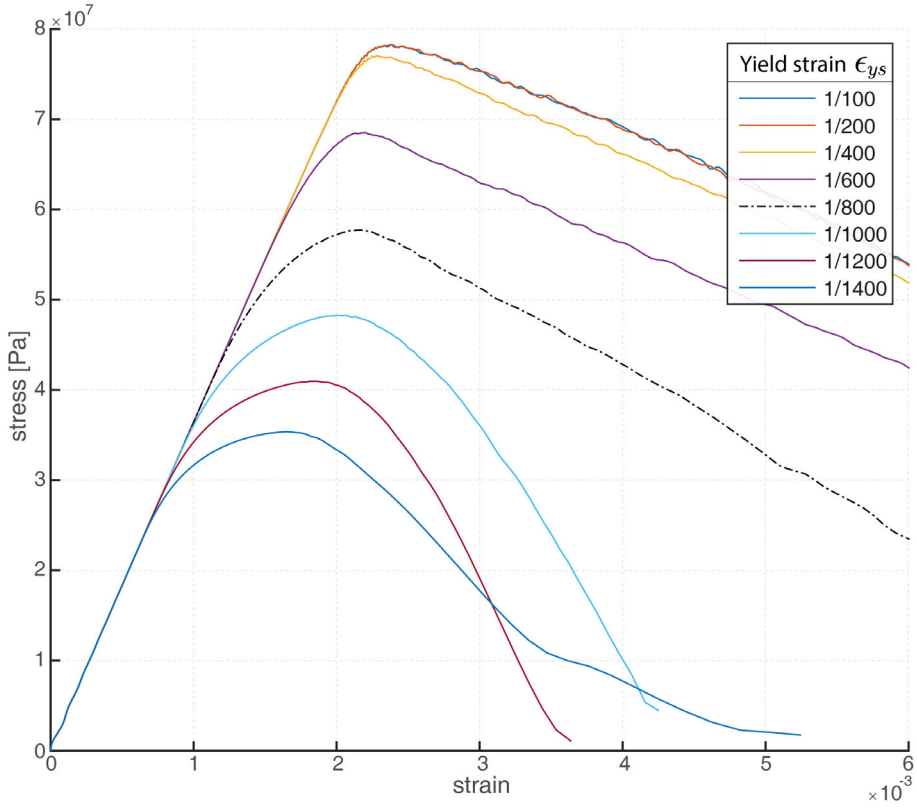

FIGURE 14 Stress-strain curves obtained from the concrete cylinder compression test with eight different values for the yield strain o_{ys}.

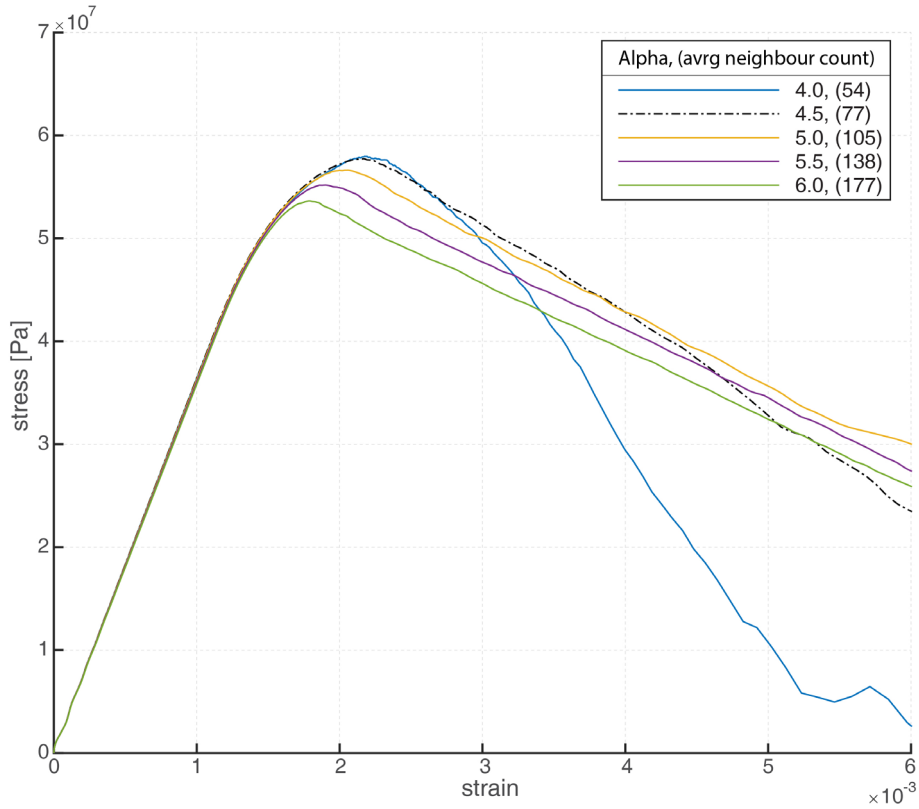

FIGURE 15 Stress-strain curve for concrete obtained from the compression cylinder test where the α parameter which controls the horizon size is varied. The resulting average number of neighbors is included in the legend.

time integration scheme based on the central difference method. The velocity of the particles are damped with a carryover factor of 0.98 to dissipate energy to reach convergence. In other words, the velocities from a previous time step are multiplied with 0.98 in each cycle. The aim is to critically damp that the fundamental mode of

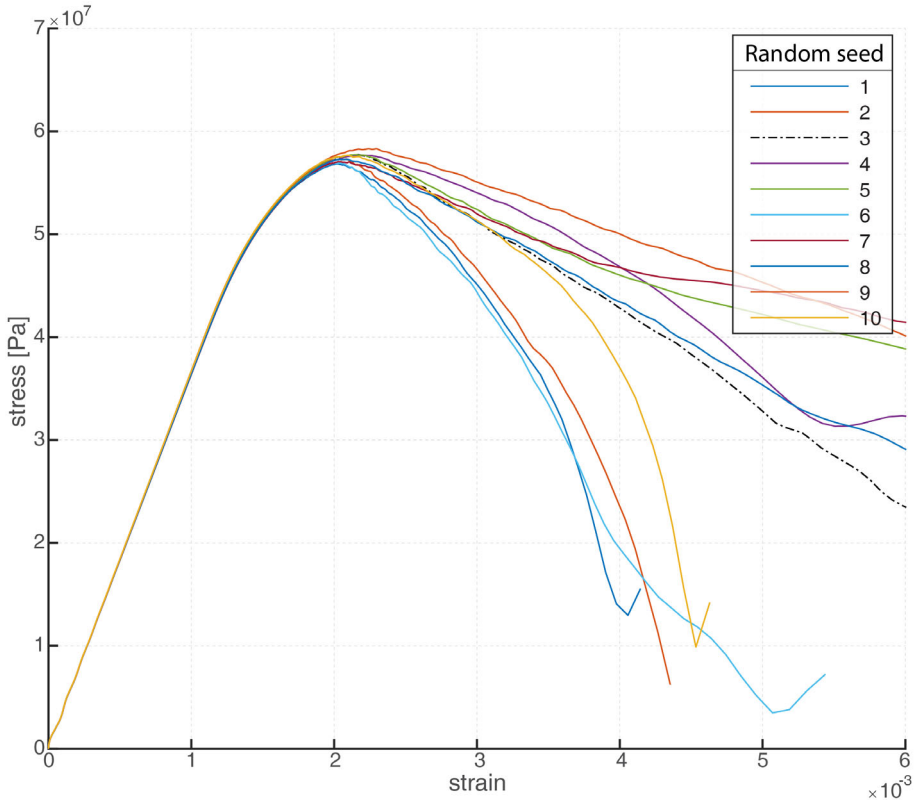

FIGURE 16 Stress-strain curve for concrete obtained from the compression cylinder test where the random seed for the shaking is varied.

oscillation. Experience shows that for larger models a number nearer 1.0 should be used. For more details on the numerical solver the reader is referred to Reference 33 (section 8.1) where the central difference scheme for peridynamics simulations is introduced in a 12 step procedure.

6.2 | Model parameters

The material model properties for the concrete and steel tests can be found in Table 1. The k parameter is used to define the shape of the kernel (see section 10 in Reference 20), ν is the Poisson's ratio, ρ the density, α is used to define the particle horizon see Reference 20, E, K, G are the Young's, the bulk and the shear modulus, respectively, ϵ_{ys} is the yield strain and δ is the elongation limit. Furthermore, the k_{spring} is the load spring stiffness, the L_{spring} refers to the initial length of the load springs and Δt is the time step.

6.3 | Parameter sensitivity study

In order to control the brittleness of the concrete, parameters such as the plastic elongation limit δ and the yield strain ϵ_{ys} which are illustrated in Figure 8 need to be specified. These parameters set the limit for how much an arm can be stretched until it starts yielding and how much further it can be stretched until it breaks. By varying ϵ_{ys}, the peak strength of the material changes as can be seen in Figure 14. However, the variation of ϵ_{ys} also has an impact on the softening. Lower values results in softer peak, less abrupt failure whereas, larger values results in a sharper peak and thus a more abrupt failure.

The variation of δ as shown in Figure 13 also has a slight impact on the peak strength, but more importantly seems to affect the brittleness. Larger values of δ results in a softer stress–strain curve whereas smaller values showcase a more sudden failure and a sharper more well-defined peak. The variation of the horizon parameter α as shown in Figure 15 also has an impact on the stress–strain curve, but not to a great extent. One could expect some changes in the behavior when the number of neighbors per particle goes from an average of 54 ($\alpha = 4.0$) to an average of 177 ($\alpha = 6.0$), and the tendency is that a larger horizon results in a lower peak strength. However, the change in peak strength in this case is <10% for a 320% change in average neighbor count, and most importantly the slope in the elastic zone (Young's modulus) is not affected.

The forth parameter that is varied is the random seed used in the particle shaking. A different seed results in a different particle distribution based on the approach

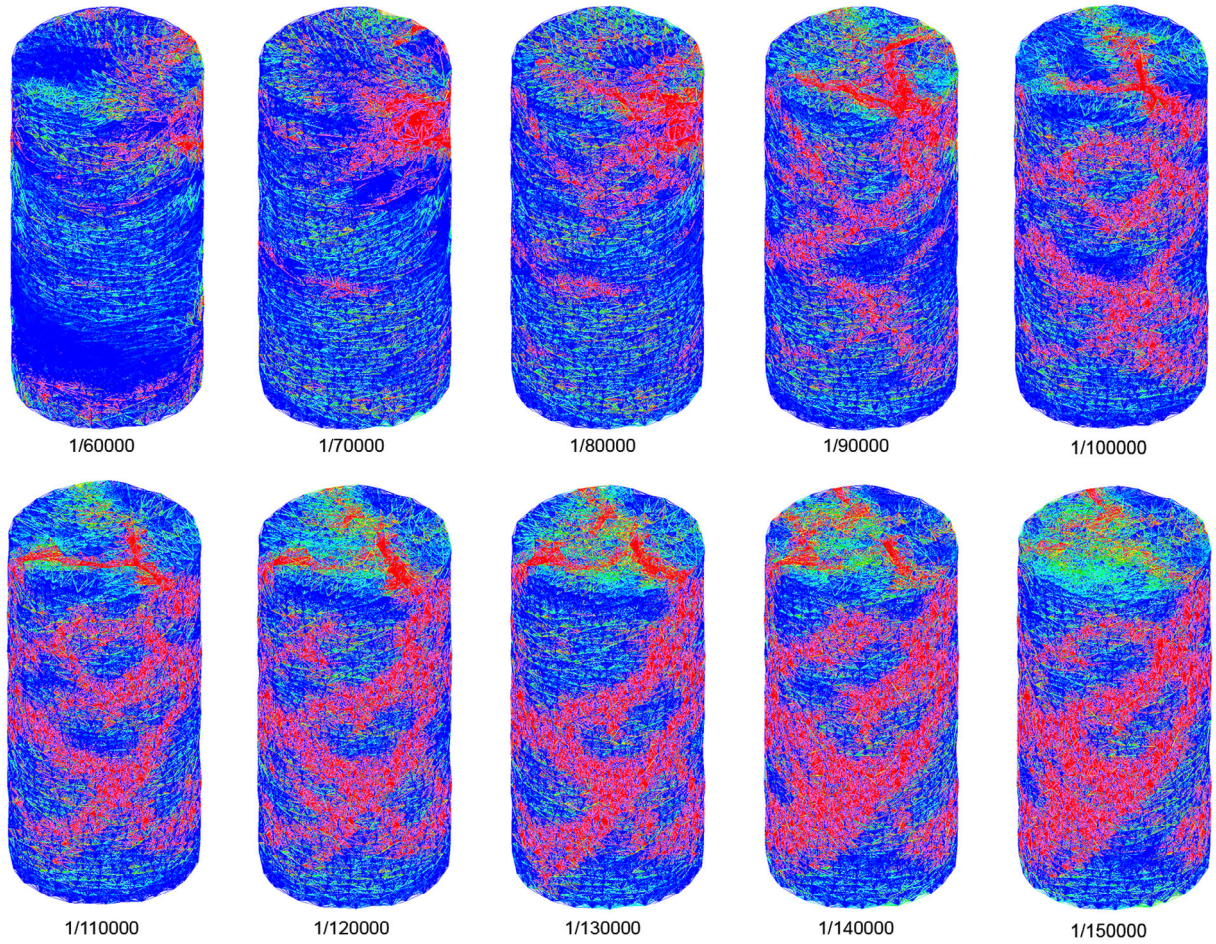

FIGURE 17 Orthographic perspective view of the failure modes for the compression cylinders where the arms are colored based on plastic elongation limit. Blue arms are still in the elastic range and red arms are stretched to failure. The numbers represent the value of δ and the stress-strain results can be seen in Figure 13.

described in Figure 12. Whereas the random seed number does not seem to effect the peak strength or the softening behavior to a large degree, it does effect the post peak shape of the stress–strain curve as shown in Figure 16. Different seed number result in slightly different failure modes since the weakness that triggers fracture occur in different places each time.

6.3.1 | Parameter choice

Table 1 lists the selection of parameters that are used to recreate a structural concrete mix that have a compression strength close to 60 MPa which is used to in the rest of the simulations. The parameters in bold font represents the choices made from the study results presented in Figures 13–16. Each of the parameters are also marked with a black dashed line in the same figures. The choice of parameters is to some extent arbitrary since there is no real concrete that this study aim to replicate. The choices have been made to reproduce a high strength concrete which has a well-defined peak in the stress–strain curve and a fracture pattern that looks believable. The results in terms of fracture pattern and failure mode for the study with varying elongation limit can be seen in Figures 17 and 18. A smaller elongation limit (i.e., the bottom row) show a damage that is more evenly spread and grows more gradually. In the case with a larger elongation limit (top row) on the other hand the failure is more explosive and localized. To further validate the model based on the combined parameters from Tables 1 and 2, the compression cylinder is also used as a test case to estimate Young's modulus and Poission's ratio, and the results can be seen in Figure 19.

6.4 | Simulations

6.4.1 | Compression cylinder

The cylinder compression test is modeled according to the dimensions in Reference 24 where the neoprene caps are modeled with a layer of springs in-between the

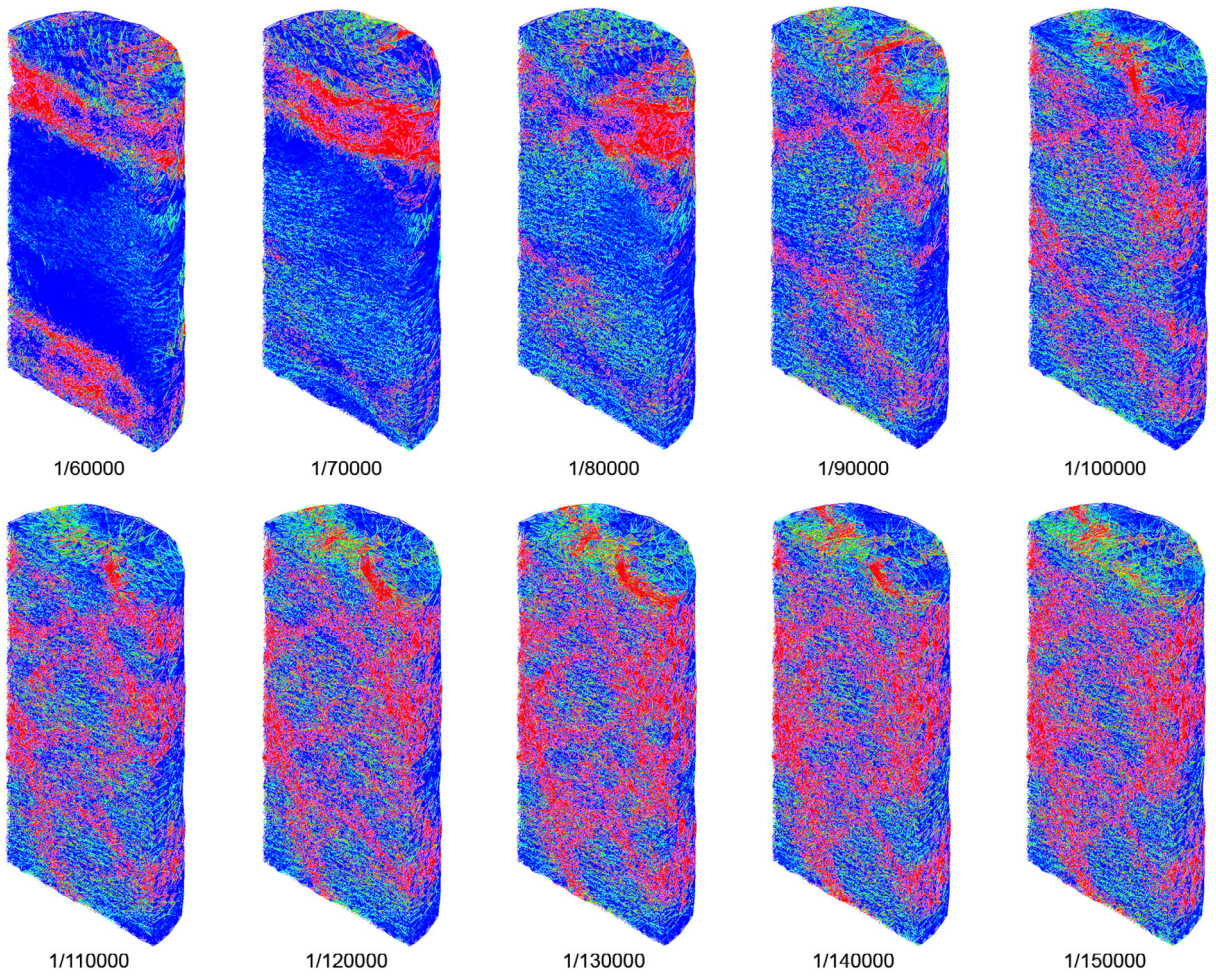

FIGURE 18 Vertical section through the compression cylinders in Figure 17 where the internal spreading of cracks can be seen.

particles that represent the concrete and the loading plates. Additional details for the setup can be found in Table 2 1.0^{-6} m per load step. After the simulation is run based on the parameters chosen in Section 6.3.1 the resulting fractured specimen can be seen in Figure 20, indicating failure along a shear surface.

The total spring force that is reached before the specimen collapses is $P_{\max} = 1.03$ MN, which is then used to compute the compressive strength σ_c according to,

$$\sigma_c = \frac{P_{\max}}{\pi r^2}, \tag{9}$$

where r is the radius of the cylinder given in Figure 1. The maximum compression strength was found to be $\sigma_c = 57.7$ MPa.

6.4.2 | Split cylinder

The split cylinder tension test is modeled according to the dimensions in Reference 27, the numerical setup is illustrated in Figure 2 and additional details can be found in Tables 1 and 2.

During the simulation, the loading plates in Figure 2 are moved towards the center of the specimen in the z-direction, as indicated with the arrows, with a rate of 1.5^{-6} m per load step. The compressive load produces a large localized compressive stress which is balanced by a horizontal tensile stress. The cylinder, therefore splits into two halves when the tensile capacity is exceeded.

The maximum applied force $P_{\max}$ is obtained by summing all the force in the load springs on one side of the specimen and the resulting tensile strength σ_t is then calculated from

$$\sigma_t = \frac{2P_{\max}}{\pi LD}, \tag{10}$$

where L is the length of the cylindrical specimen in meters and D is the diameter of the cylinder.[27] The total spring force that was reached in the simulation is $P_{\max} = 1.15$ MN resulting in a maximum tensile strength of $\sigma_t = 16.2$ MPa. The fractured mode as shown in

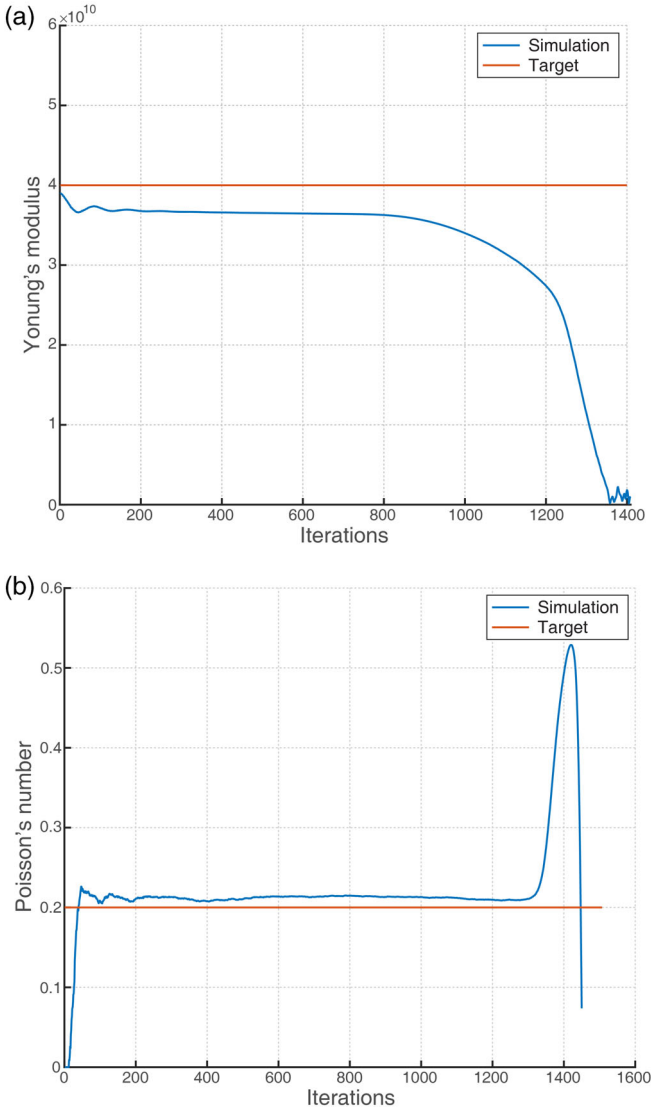

FIGURE 19 Young's modulus and Poisson's ratio for concrete as retrieved on the macro scale, compared with the values given on the particle scale. The prediction of these quantities is best when the material is still in the elastic zone and fails as the specimen collapses.

Figure 21 exhibits a vertical crack through the center of the cylinder which effectively splits the cylinder in half. The specimen on the right in Figure 21 shows the typical Y-shaped crack branching around the area where the load is applied.

6.4.3 | Modulus of rupture

The Modulus of rupture test is modeled according to the proportions suggested in Reference 32. The numerical setup of the physical test is illustrated in Figure 3. Each of the two loading plates is moved in the direction of the large arrows in Figure 3 in a rate of 4×10^{-7} m per load step. The two top cylinders introduce two point loads to the beam, resulting in a constant bending moment with tension in the bottom layer between these two points. The failure can be expected to take place somewhere in this zone, and the precise placement will be dictated by the random arrangement of particles.

The maximum load $P_{\max}$ is calculated by adding all the force in the springs on either the upper side or lower side of the specimen. The tensile strength σ_t is then calculated from

$$\sigma_t = \frac{P_{\max} L}{bd^2}, \tag{11}$$

where L is the length, b is the breadth and d is the depth of the beam. The total spring force $P_{\max}$ that was reached in the simulation was $P_{\max} = 0.11$ MN resulting in a maximum tension strength of $\sigma_t = 22.7$ MPa. The fractured specimen as shown in Figure 22 shows that the cracks are initiated in-between the two loading cylinders at the top, as expected.

6.4.4 | Direct tension

The direct tension test is setup as a cylindrical object with a waist that has half the diameter of the wider ends as shown in Figure 4. The loading plates are moved in the x-direction away from the center of the specimen at a rate of 1.8^{-7} m per load step. The tensile stress will be higher in the narrow waist of the specimen since it has a smaller cross-section area, so failure is expected to happen there. The maximum force $P_{\max}$ is calculated by summing the spring force on one side of the specimen. The tensile strength σ_t is then calculated from

$$\sigma_t = \frac{P_{\max}}{\pi r^2}, \tag{12}$$

where $P_{\max}$ is the maximum registered load before failure and r is the radius at the waist of the specimen. The total spring force that was reached in the simulation is $P_{\max} = 0.10$ MN resulting in a maximum tensile strength of $\sigma_t = 22.6$ MPa. The fractured specimen as shown in Figure 23 indicates that the failure happens at the waist as expected. A cross-section of the fracture specimen at $y = 0$, is shown in Figure 24 where it can be observed that the crack on the left side seems to be the one that lead to failure.

6.5 | Comparison

Figure 25 shows a compilation of how the stress developed with the incremental load steps for each of the four concrete test cases. The peak value represents the

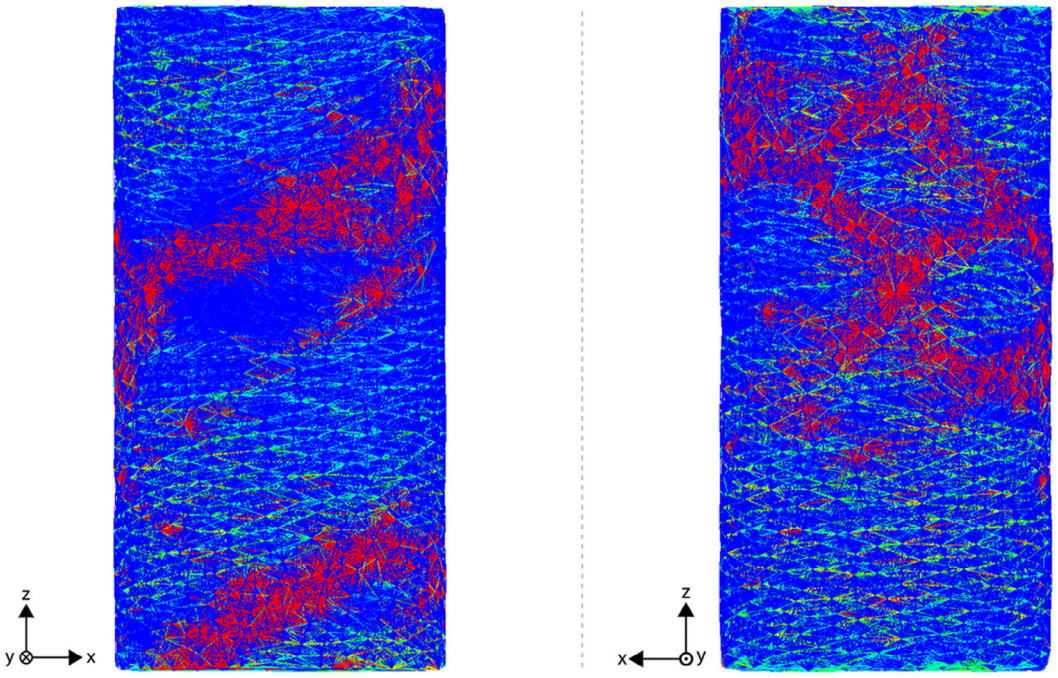

FIGURE 20 Front elevation to the left and rear elevation to the right of the fractured compression cylinder. The arms are colored by plastic elongation, where red arms are stretched to failure and blue arms are intact.

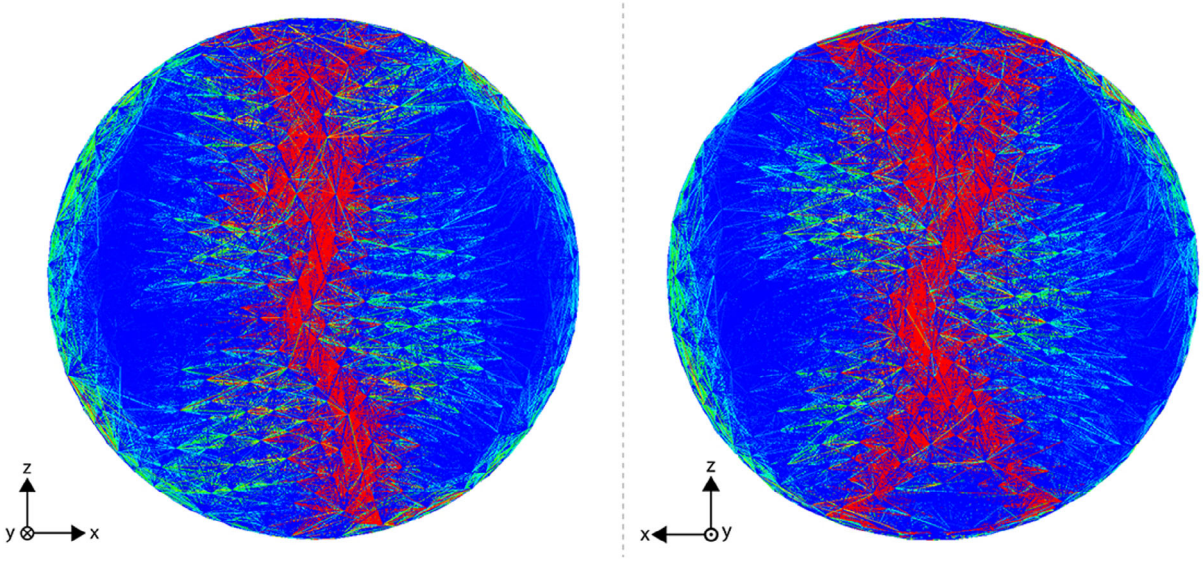

FIGURE 21 Showing the front and rear elevation of the split cylinder after the fracture has occurred. The arms are colored by plastic elongation, where red arms are stretched to failure and blue arms are intact.

strength for each test case, and the stress is calculated from Equation (9) for the cylinder compression test, Equation (10) for the split cylinder, Equation (11) for the modulus of rupture and Equation (12) for the direct tension test. The reference value for the tension strength which is marked with a dashed line is taken from Reference 21 where it is postulated to be 10% of the compression strength (Figure 25).

6.6 | Simulation of steel reinforcement

To wrap up this study a model which is similar to the concrete testing is setup to simulate the testing of steel reinforcement according to ASTM 370.[34] The parameters for the model can be found in Tables 1 and 2 and the dimension for the specimen can be seen in Figure 5. The specimen is loaded by moving the loading plates in the x-

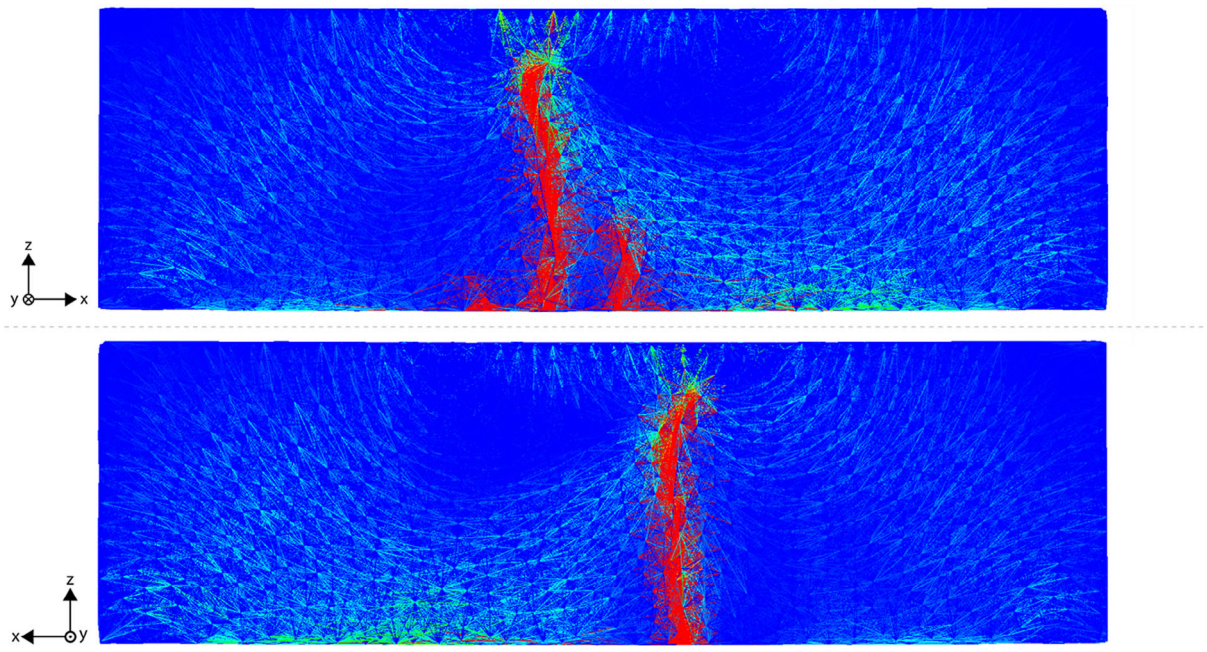

FIGURE 22 Front elevation above, and rear elevation below, of the modulus of rupture beam after fracture has occurred. The arms are colored by plastic elongation, where red arms are stretched to failure and blue arms are intact.

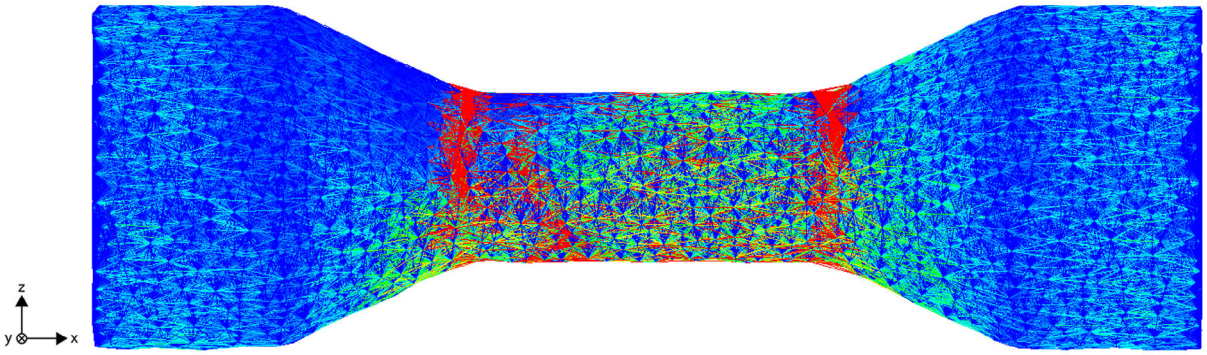

FIGURE 23 Front elevation of the 3D concrete specimen after fracture has occurred. The arms are colored by plastic elongation where red arms are broken and blue arms are intact.

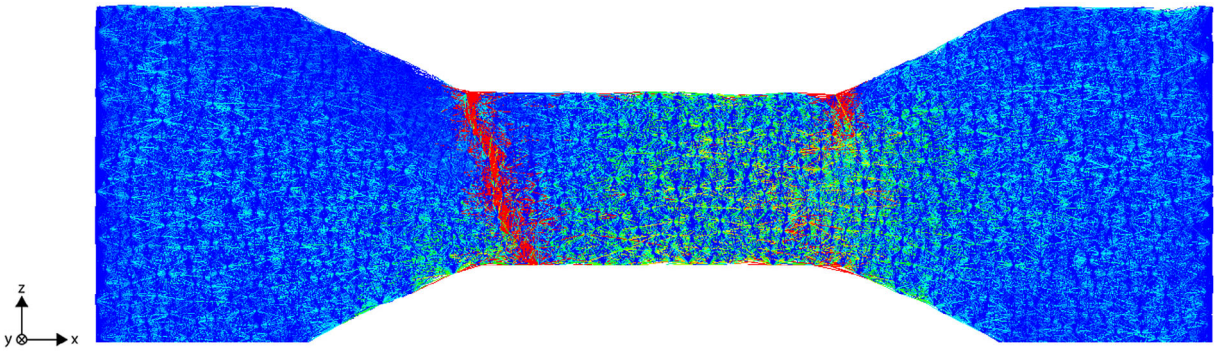

FIGURE 24 Showing a section cut through the concrete specimen with an xz-plane at $y = 0$. Arms colored by plastic elongation where red arms are broken and blue arms are intact. The left crack shown in Figure 23 can be seen to cut all the way through the object and is most likely what lead to failure.

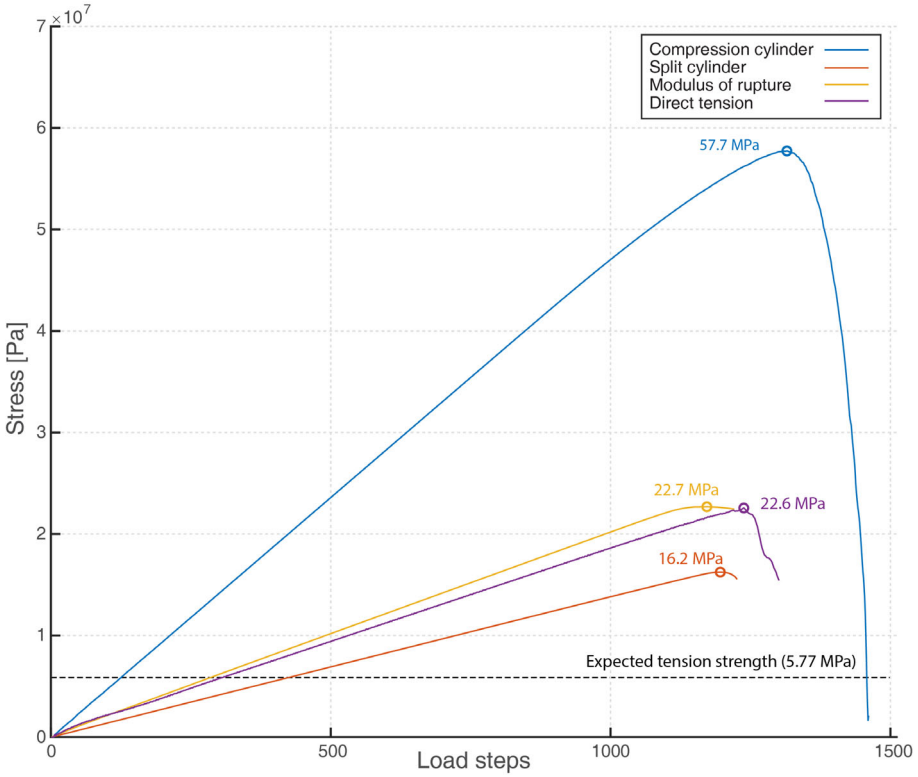

FIGURE 25 Comparing the results of the compression test and the three different tension tests. The reference value for the expected tension strength is based on the conclusion from [14], where the tensile strength is found to be approximately 10% of the compression strength.

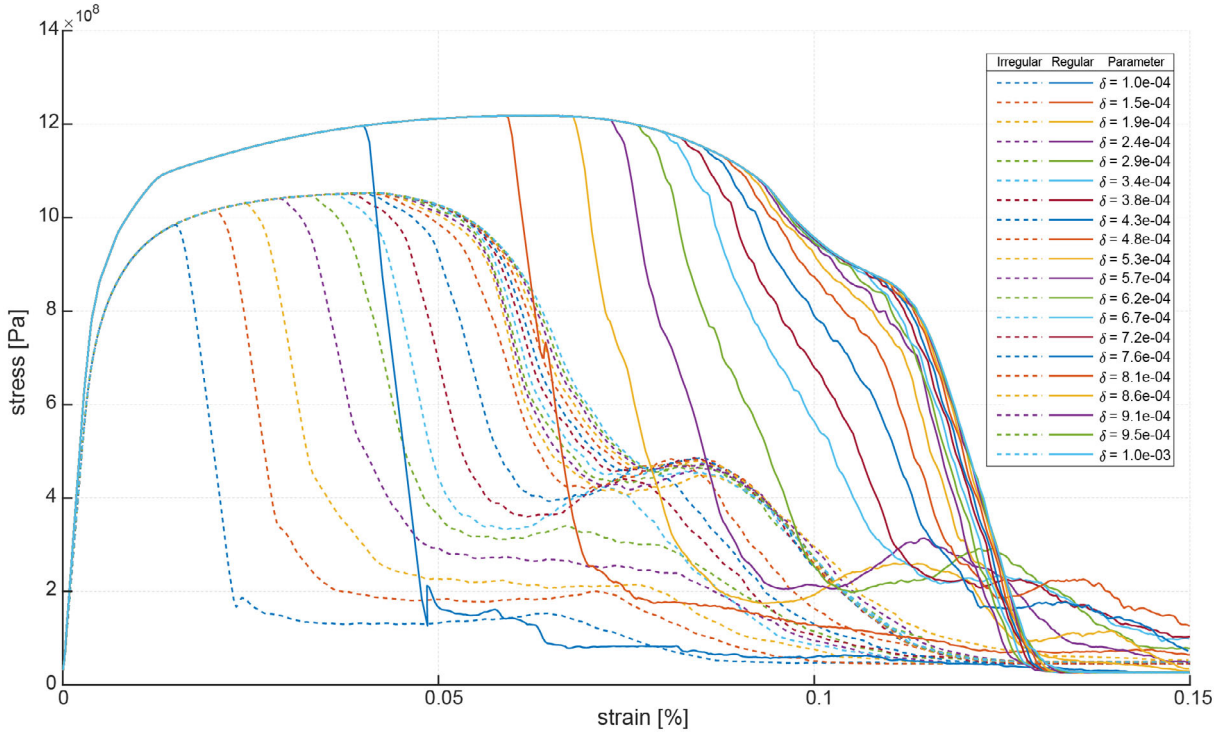

FIGURE 26 Stress-strain curves for steel using regular and irregular particle distribution where the plastic elongation limit δ is varied and the yield strain is kept constant at $o_{ys} = 0.0028$.

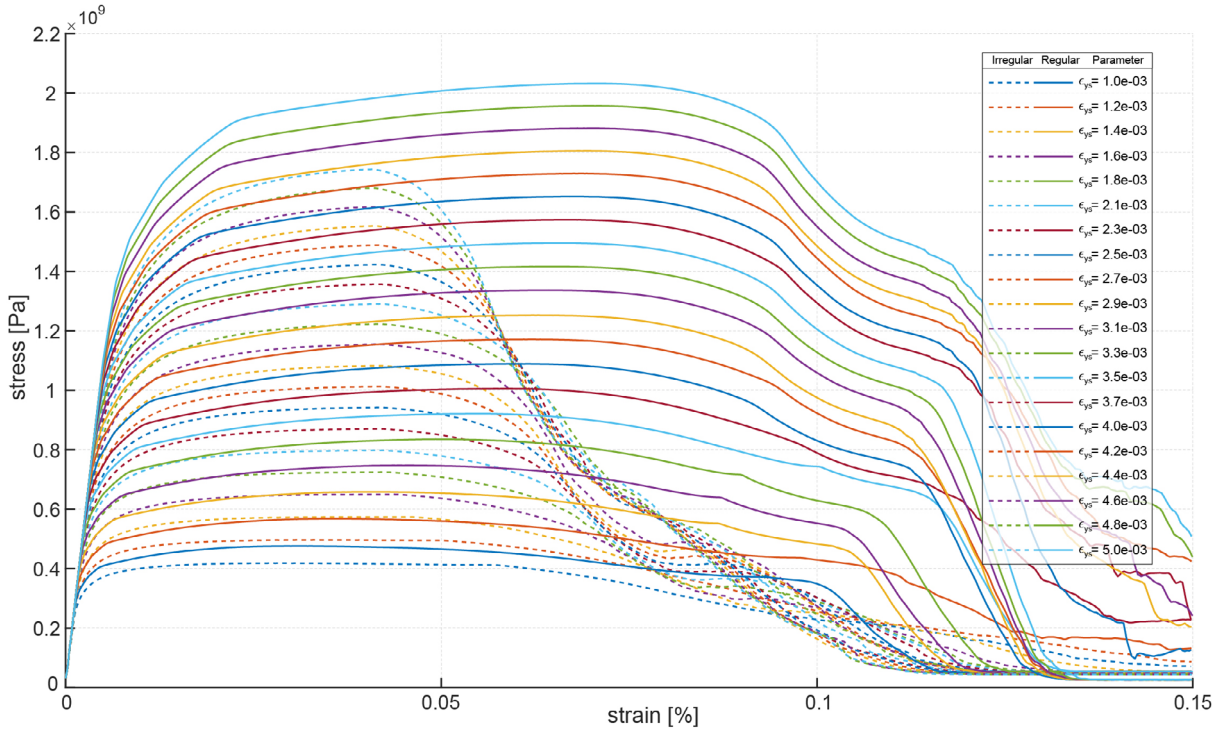

FIGURE 27 Stress-strain curves for steel using regular and irregular particle distribution where the yield strain parameter o_{ys} is varied and plastic elongation limit is kept constant at $\delta = 0.001$

direction away from the origin at a rate of 7^{-8} m per load step. The strain is calculated by measuring the difference in the average movement of the particles at an *yz*-plane at $x = -0.025$ and $x = 0.025$ m and dividing the retrieved extension by the initial distance between the planes which is 0.05 m, see Figure 5.

Since steel is a rather homogeneous material compared with concrete, the simulations are run for both regular and irregular particle distribution. The imperfections caused by the irregular distribution turned out to concentrate large parts of the strain around the weakest area of the specimen and smaller total strain levels were reached compared with the regular distribution where the strain was distributed over larger parts of the specimen. This can be seen in Figure 26 where the continuous lines represent simulations with regular particle distribution and dashed lines represent simulations with irregular particle distribution for the same variation of the plastic elongation limit δ.

As expected the variation of δ controls the brittleness/ductility of the steel as can be seen in Figure 26 where a larger δ results in a more ductile steel but these results are also affected significantly by the choice of particle arrangement. The variation of ϵ_{ys} on the other hand moves the stress–strain curves vertically in Figure 27 and thus has a major influence on the peak strength.

7 | DISCUSSION AND CONCLUSIONS

The present study showed an application of a macro model based on force flux peridynamics theory to simulate structural concrete behavior. This was done by recreating the physical concrete tests—such as the compression cylinder, the split cylinder, the modulus of rupture test and the direct tension test—with a numerical setup. The cylinder compression test was used to verify that the model would recreate Young's modulus and Poisson's ratio with reasonable accuracy. A set of parameters were chosen to recreate a typical high strength concrete and three different tensile tests were carried out to evaluate the resulting tensile strength. The following observations were made:

- By varying the plastic elongation limit, the yield strength and the particle horizon, a variety of characteristic stress–strain curves can be obtained, showing a promising capability for modeling different concrete mixes.
- The plastic elongation limit has an impact on both the softening but also on the peak stress. The yield strain and the horizon size mainly affect the peak stress, which is also affected to a smaller degree by the random seed number.

- The results from the tension strength tests show that the numerical material model is significantly stronger compared with typical physical test results. That could perhaps be explained by the lack of imperfections in the model such as small cracks.
- Comparing the results from the three different tension tests, the modulus of rupture gives the highest prediction and the split cylinder the lowest. It is generally accepted that the modulus of rupture strength is the greatest in physical tests, possibly because the maximum tensile stress occurs in a small proportion of the sample.
- The simulation of the steel test shows the potential of using this model for both concrete and steel. It also highlights the impact that the particle arrangement has on both the strength and the strain for a ductile material.

The present macro implementation of FFPD is limited by modeling one single smeared constituent which could be an explanation for the overestimate of tensile strength. Hence the re-implementation of FFPD as a mesoscale model could be one way to develop the study further. Another way could be to weaken the material in tension for the macro scale implementation by introducing imperfections. Further studies could also include modeling of the bond interface between concrete and steel for the implementation of FFPD to RC structures.

ACKNOWLEDGMENT

We greatly appreciate financial support from the Chalmers Foundation and the Swedish research councils: Formas, Vinnova and Energimyndigheten in the project Smart Built Environment: Digitalisering och industrialisering för ett hållbart samhällsbyggande 2019.

DATA AVAILABILITY STATEMENT

The data that support the findings of this study are available from the corresponding author upon reasonable request.

ORCID

Jens Olsson https://orcid.org/0000-0001-9470-0566

REFERENCES

1. Fan W, Chen Y, Li J, Sun Y, Feng J, Hassanin H, et al. Machine learning applied to the design and inspection of reinforced concrete bridges: resilient methods and emerging applications. Structures. 2021;33:3954–63. https://doi.org/10.1016/j.istruc.2021.06.110
2. Bažant ZP, Tabbara MR, Kazemi MT, Pijaudier-Cabot G. Random particle model for fracture of aggregate or fiber composites. J Eng Mech. 1990;116(8):1686–705. https://doi.org/10.1061/(ASCE)0733-9399(1990)116:8(1686)
3. Thilakarathna PSM, Kristombu Baduge KS, Mendis P, Vimonsatit V, Lee H. Mesoscale modelling of concrete: a review of geometry generation, placing algorithms, constitutive relations and applications. Eng Fract Mech. 2020;231:106974. https://doi.org/10.1016/j.engfracmech.2020.106974
4. Ren W, Yang Z, Sharma R, Zhang C, Withers PJ. Two-dimensional X-ray CT image based meso-scale fracture modelling of concrete. Eng Fract Mech. 2015;133:24–39. https://doi.org/10.1016/j.engfracmech.2014.10.016
5. Javili A, Morasata R, Oterkus E, Oterkus S. Peridynamics review. Math Mech Solids. 2018;24(11):3714–39. https://doi.org/10.1177/1081286518803411
6. Miranda HD, Orr J, Williams C. Fast interaction functions for bond-based peridynamics. Eur J Comput Mech. 2018;27(3):247–76. https://doi.org/10.1080/17797179.2018.1547356
7. Silling SA. Reformulation of elasticity theory for discontinuities and long-range forces. J Mech Phys Solids. 2000;48(1):175–209. https://doi.org/10.1016/S0022-5096(99)00029-0
8. Gerstle W, Sau N, Silling S. Peridynamic modelling of concrete structures. Nucl Eng Des. 2007;237(12–13):1250–8. https://doi.org/10.1016/j.nucengdes.2006.10.002
9. Gerstle W, Sau N, Sakhavand N. On peridynamic computational simulation of concrete structures. ACI Special Publ. 2009;65:245–64.
10. Yaghoobi A, Chorzepa MG. Fracture analysis of fiber reinforced concrete structures in the micropolar peridynamic analysis framework. Eng Fract Mech. 2017;169:238–50. https://doi.org/10.1016/j.engfracmech.2016.11.004
11. Huang D, Zhang Q, Qiao PZ. Damage and progressive failure of concrete structures using non-local peridynamic modeling. Science China Technological Sciences. 2011;54(3):591–6.
12. Shen F, Zhang Q, Huang D. Damage and failure process of concrete structure under uniaxial compression based on Peridynamics modeling. Math Probl Eng. 2013;2013:631074.
13. Huang D, Guangda L, Liu Y. Nonlocal peridynamic modeling and simulation on crack propagation in concrete structures. Math Probl Eng. 2015;2015:1–11. https://doi.org/10.1155/2015/858723
14. Hattori G, Hobbs M, Orr J. A review on the developments of peridynamics for reinforced concrete structures. Arch Comput Methods Eng. 2021;28(7):4655–86. https://doi.org/10.1007/s11831-021-09549-y
15. Baranowski P, Kucewicz M, Małachowski J, Sielicki PW. Failure behavior of a concrete slab perforated by a deformable bullet. Eng Struct. 2021;245:112832. https://doi.org/10.1016/j.engstruct.2021.112832
16. Patel P, Bodda SS, Gupta A. Modeling the behavior of reinforced concrete slabs subjected to impact. Nucl Eng Des. 2021;385:111512. https://doi.org/10.1016/j.nucengdes.2021.111512
17. Rabczuk T, Eibl J. Simulation of high velocity concrete fragmentation using SPH/MLSPH. Int J Numer Methods Eng. 2003;56(10):1421–44. https://doi.org/10.1002/nme.617
18. Huˇsek M, Kala J, Král P, Hokeš F. Steel fibre reinforced concrete simulation with the SPH method. IOP Conf Ser Mater Sci Eng. 2017;245:032070. https://doi.org/10.1088/1757-899x/245/3/032070
19. Kulasegaram S, Karihaloo BL, Ghanbari A. Modelling the flow of self-compacting concrete. Int J Numer Anal Methods Geomech. 2011;35(6):713–23. https://doi.org/10.1002/nag.924
20. Olsson J, Ander M, Williams CJK. The use of peridynamic virtual fibres to simulate yielding and brittle fracture. J Peridyn

Non-Local Model. 2021;3:348–82. https://doi.org/10.1007/s42102-021-00051-4
21. Raphael JM. Tensile strength of concrete. J Proc. 1984;81(2):158-165.
22. Grassl P, Jirásek M. Damage-plastic model for concrete failure. Int J Solids Struct. 2006;43(22):7166–96. https://doi.org/10.1016/j.ijsolstr.2006.06.032
23. Hannant DJ, Buckley KJ, Croft J. The effect of aggregate size on the use of the cylinder splitting test as a measure of tensile strength. Mater Sci. 1973;6(1):15–21. https://doi.org/10.1007/bf02474838
24. ASTM. ASTM standard test method for compressive strength of cylindrical concrete specimens. West Conshohocken, PN: American Standard Test Method; 2009.
25. Zdenek BP, Taghi KM, Toshiaki H, Jacky M. Size effect in Brazilian Split-cylinder tests: measurements and fracture analysis. Mater J. 1991;88:325–32.
26. Carneiro FLL, Aguinaldo B. Tensile strength of concrete. RILEM Bull. 1953;13:97–123.
27. ASTM C 496/C 496M-04. Standard test method for splitting tensile strength of cylindrical concrete specimens. West Conshohocken, PN: American Standard Test Method; 2004.
28. Timoshenko S, Goodier JN. Theory of elasticity. New York: McGraw-Hill Book Co.; 1951.
29. Kim JJ, Taha MR. Experimental and numerical evaluation of direct tension test for cylindrical concrete specimens. Adv Civ Eng. 2014;2014:1–8. https://doi.org/10.1155/2014/156926
30. Gingold RA, Monaghan JJ. Smoothed particle hydrodynamics: theory and application to non-spherical stars. Month Notices Roy Astronom Soc. 1977;181:375–89. https://doi.org/10.1093/mnras/181.3.375
31. Silling SA, Epton M, Weckner O, Xu J, Askari E. Peridynamic states and constitutive modeling. J Elast. 2007;88:151–84.
32. ASTM C 78-02. Standard test method for flexural strength of concrete (using simple beam with third-point loading). West Conshohocken, Penn, USA: American Standard Test Method; 2002.
33. David J. Littlewood. Roadmap for Peridynamics implementation. Tech. Rep. Sandia National Laboratories, 2015.
34. ASTM. Standard test methods and definitions for mechanical testing of steel products. West Conshohocken, PN: American Standard Test Method; 2016.

AUTHOR BIOGRAPHIES

Jens Olsson Phd student at Chalmers University of Technology, Department of Architecture and Civil Engineering, Architectural Theory and Methods.

Mats Ander Senior Lecturer at the Division of Material and Computational Mechanics, Department of Industrial and Materials Science at Chalmers University of Technology.

Chris J. K. Williams Artistic Professor at Chalmers University of technology, Department of Architecture and Civil Engineering, Architectural Theory and Methods.

How to cite this article: Olsson J, Ander M, Williams CJK. The numerical simulation of standard concrete tests and steel reinforcement using force flux peridynamics. Structural Concrete. 2022. https://doi.org/10.1002/suco.202200153